MDPI

Article

Tensor-based Factorization Algorithms for Pixel-wise Classification of Hyperspectral Data Using Deep Convolutional Networks

Josué López [1,*], Deni Torres [1] and Clement Atzberger [2]

[1] Center for Research and Advanced Studies of the National Polytechnic Institute, Telecommunications Group, Av del Bosque 1145, Zapopan 45017, Mexico; dtorres@gdl.cinvestav.mx
[3] University of Natural Resources and Life Science, Institute of Geomatics, Peter Jordan 82, Vienna 1180, Austria; clement.atzberger@boku.ac.at
* Correspondence: josue.lopez@cinvestav.mx

Version November 9, 2020 submitted to Remote Sens.

Abstract: Tensor-based algorithms for data compression have evolved in recent years according to the needs of several research areas. Tucker Decomposition (TKD) is one of the most popular factorization methods based on tensor algebra, but it is clear that it is not the only algorithm wich can produce a factorization for a given input data set. Besides, this decomposition does not have singular solutions, i.e., it converges to local minima. Hence, depending on the input data, tensor-based decompositions can achieve better solution to a specific input. The phenomenology of Remote Sensing (RS) Hyperspectral Images (HSI) belongs to the set of natural numbers, i.e., the set of positive integers. Then, a non-negative tensor factorization suggest a more suitable decomposition for positive data by nature. The main purpose of this work is to prove the benefits in processing time, as well as in accuracy, of using a well-posed factorization algorithm. Specifically, this paper performs a quantitative analysis of tensor-based factorization algorithms applied to semantic segmentation of HSI using Deep Convolutional Networks (DCN).

Keywords: deep convolutional networks; hyperspectral imagery; tensor decomposition

1. Introduction

Reducing the dimensionality of input data for machine learning algorithms has been one of the most active research areas in ~~recente~~ recent years []. The insertion of tensor-based algorithms for ~~this sort of tasks drove a revolution~~ these types of tasks inspired a change in several areas, such as image processing. [].

Most of the researchs in the image processing area require data acquired by multiple sensors. Even in the simplest case, color images, data acquired by three sensors that perceive reflectance of an object are processed. Each sensor receives reflectance in different wavelength ranges, and by merging that data, a color image is produced. Thus, the images can be represented in a form of three-dimensional arrays or third-order tensors. Two dimensions represent the spatial properties and the third dimension denotes the depth, i.e., the spectral bands. Medical analysis [], minorology [], agriculture, [], radar images [] and, above all, remote sensing multi- and hyper-spectral images [] can be represented, by nature, as third-order tensors.

Spectral ~~imagery remarkably aids~~ images make certain image processing tasks much easier []. Recently, the use of this type of data has grown exponentially in various areas such as agriculture [], medical analysis [], biomedical [], natural disaster prediction [], security affairs [], among others. The ability to obtain information about a target not only by its reflectance in the spatial domain, but also

by response at different wavelengths, has driven a growth in accuracy and precision in tasks such as classification and segmentation [].

Few years ago, several unsupervised classification and segmentation algorithms [] were developed, taking advantage of the properties that spectral data produce. Subsequently, with the introduction of supervised machine learning algorithms such as SVM [], kNN [] and ANN [], it was found that, under certain conditions, there is a direct relationship between the number of bands used and the performance of these algorithms []. However, with the aim of improving results, neural network models evolved into deep neural networks []. This caused the computational complexity to rise considerably and spectral image processing was not easily achievable. The foregoing requires having robust computer equipment to achieve competitive results in time.

Several works opted for matrix factorization algorithm to reduce the high-dimensionality of spectral images []. More recently, with the development of tensor factorization algorithms [], it has been found that some algorithms based on tensor algebra produce advantages over those based on matrices []. Nevertheless, the data produced by both of them are hard to understand for supervised classification algorithms that need spatial relation between pixels to produce a wise prediction [].

In this work, ~~we propose~~ the proposal is to find an alternative solution to the problem described previously. ~~To reduce processing times in supervised classification algorithms, such as deep neural networks, we~~ We propose a model that ~~, from the benefits offered by tensor decomposition algorithms, aids compression of spectral images~~reduces the computational load of hyperspectral imagery classification supervised algorithms through tensor decomposition models. This produces a lower dimensional tensor while preserving the structural and numerical nature of the original data.

1.1. ~~State of the art~~Previous work

There are several works focused on the development of frameworks that reduce computational complexity of machine learning algorithms for semantic segmentation of hyperspectral datasets []. The crucial factor, which is addressed in this work, is to achieve compression of the input data to reduce the high number of computatios, but without sacrificing pixel accuracy, overall accuracy, precision and recall in the classification task.

Before the introduction of tensor decomposition algorithms, the way to use hyperspectral images as input for supervised classification algorithms was by band selection [23] and [22]. Later, matrix decomposition algorithms were used, such as PCA in [**?**], and even non-negative matrix decomposition methods [**?**]. In 2015 Zhang et al. [24] were pioneers in experimenting with multilinear algebra-based decompositions on hyperspectral images.

On the other hand, there was also the possibility of using multispectral images due to the small number of spectral bands, which still made efficient results in classification without dimensionality reduction achievable, as done in [11], [18], [21] and [**?**]. However, the need to increase classification performance forces researchers to use data with more features that favor and aid the classification of various classes, which are difficult to differentiate with little spectral data. Thus, more recent researchs have decided to use hyperspectral images with tensor decompositions, which has increased the results in classification accuracy [26], [27], [29], [**?**] and [**?**].

Recently, Sayeh et al. [**?**] published a work close to our research. They proposed a non-negative tensor decomposition of hyperspectral images but, different to our research, they try to preserve certain spatial-spectral features into the so called abundance maps, i.e. the projection matrices, while this work pursuits to preserve the nature of the image just compressing the main information in the positive core tensor.

Table 1 summarizes some of the most cited related papers, wich deal with the compression-classification issue.

Table 1. Related work in spectral imagery semantic segmentation.

Reference	Input	Decomposition	Reduction	Classifier
Li, S. et al. [23] (2014)	HSI	-	Band selection	SVM
Zhang, L. et al. [24] (2015)	HSI	TKD	Spatial-Spectral	-
Wan, Q. et al. [22] (2016)	HSI	-	Band selection	SVM/kNN/CART
Kemker, R. et al. [11] (2017)	MSI	-	-	CNN
Tong L. et al. [] (2017)	HSI	NMF	Unmixing	-
Hamida, A. et al. [21] (2017)	MSI	-	-	CNN
Chien, J. et al. [] (2017)	RGB	TFNN	Spatial-Spectral	TFNN
Dewa, M. et al. [] (2018)	HSI	PCA	Spectral	PCA
Xu, Y. et al. [] (2018)	HSI	-	-	CNN
Li, J. et al. [28] (2019)	MSI	NTD-CNN	Spatial-spectral	-
An, J. et al. [27] (2019)	HSI	T-MLRD	Spatial-spectral	SVM/1NN
An, J. et al. [29] (2019)	HSI	TDA	Spatial-spectral	SVM/1NN
Lopez, J. et al. [] (2019)	MSI	TKD	Spectral	FCN
Sayeh, M. et al. [] (2019)	HSI	NTD	Spatial-Spectral	3D-CNN
Our framework	**MSI/HSI**	~~NTKD~~iNTD/NTD	**Spectral**	**CNN**

1.2. ~~Contribution~~Motivation

Nowadays, RS image processing is applied in several areas related to caring of the planet. Nevertheless, task such as classification becomes more complex due to low spatial resolutions, this is offset by the use of devices with other features such as spectral sensors.

~~In the state of the art we can find a variety of frameworks looking for dimensionality reduction of images of any type, that is , RGB [?], medical [?], SAR [?], multispectral [?], among others. In particular, the large number of spectral bands in hyperspectral images has focused efforts in this category [?]. Spatial [?], spectral [?] and spatial-spectral [?] compression have been achieved with~~ On the other hand, CNNs have been widely used in recent years in the area of RGB image semantic classification and segmentation. Its performance is highly competitive and the development of various improvement strategies have considerably reduced its computational cost []. However, the computational complexity of the algorithm means that the increase in the dimensionality of the input data produces a significant increase in the computational load []. This is why the processing of high-dimensional images such as multi and hyperspectral images becomes unfeasible.

Some data compression strategies have favorably reduced the dimensionality of the data. Decomposition methods based on the matrix and tensor ~~decompositions. It is important to highlight that, a decomposition as~~ approaches have been applied as pre-processing ~~for a classification algorithm, instead of favoring, could be counterproductive and greatly affect its performance. It is therefore important to make a proper selection of the type of decomposition that would produce a suitable data set for post-processing~~of input data of neural networks. In tensor decompositions, the processing of the data in its natural format, i.e., as N-order tensors, improves the decomposition process because it considers the dependence of the data in its different modes. Although a decomposition can compress the data, it is also important to note that the inappropriate selection of some decomposition parameters could lead to information losses, which would penalize the performance of a CNN.

Under these considerations, this work is motivated to develop a low computational complexity and competitive in performance framework that helps various fields of application of remote sensing image processing to solve classification tasks.

1.3. Contribution

Unlike previous works, this work seeks to adapt the data in ~~the best way to be~~ a more efficient way to the input of deep convolutional networks. Convolutional network models are designed to extract and interpret all the spatial properties of an image by moving the kernels over the input data []. Therefore, producing uncorrelated data in space and spectrum, would make harder the interpretation

of the data in the convolutional network [**?**]. Thus, the proposed framework maintains the ~~positive~~ integer and nonnegativity tensor nature of the spectral images and the spatial dimensionality to preserver spatial-spectral correlation of the data while reducing the spectral dimensionality, in order to decrease computational load in the pixel-wise classification process. Besides, we approach the problem of setting the compression range selection hyperparameters by the measurment of divergences, which aids to estimate a best rank approximation.

We can summarize the contribution of this work with the following two points:

1. The framework ~~NTKD3-CNN~~ INTD1-CNN proposed in this work, develops a new strategy to improve ~~accuracy results~~ performance of semantic segmentation convolutional neural networks by finding suitable tensor data, preserving spatial correlation and values in the set of the natural numbers while compressing the spectral domain and in turn decreasing computational load.
2. Furthermore, this work proposes a strategy for defining the range in mode 3 of the compression models based on the Tucker decomposition from the information theory point of view.
3. This work also presents an exhaustive performance analysis measuring and comparing its efficiency with the most popular metrics, i.e., as pixel accuracy (PA), also PA in function of the number of new tensor bands, precision, recall, F1, orthogonality degree of the factor matrices and the core tensor, reconstruction error of the original tensor, and execution time.

The remainder of this work is organized as follows. Section **??** introduces tensor algebra notation and basic concepts to familiarize the reader with the symbology used in this paper. Section **??** presents the problem statement of this work and the mathematical definition. In Section **??**, CNN theory is described for classification and semantic segmentation. Section **??** presents the framework proposed for compression and semantic segmentation of spectral images. Experimental results are presented in Section **??**. Finally, Sections **??** and 8 present a discussion and conclusions based on the results obtained in the experiments.

2. ~~Tensor-Based Factorizations~~Notation and definitions

Matrix-based factorizations, such as PCA [] and SVD [] have been significant and useful tools for dimensionality reduction and other approaches. Nevertheless, they are limited ~~by representations of data in two modes~~to data representations in 2-dimensional spaces. Most of current applications have data structures often as higher-order arrays, e.g. dimensions of space, time, and frequency. This 2-way view in matrix factorizations may be inadequate and it is natural to use tensor decomposition approaches [**?**].

~~We can define a tensor~~ A tensor can be defined as a multi-way or multidimensional array. The order of a tensor is the number of dimensions, also known as modes, i.e., an N-order tensor $\mathcal{X} \in \mathbb{R}^{I_1 \times I_2 \times I_3}$ is an N-dimesional array, which elements ~~$y_{i_1,i_2,\ldots,i_n}$~~ $x_{i_1,i_2,\ldots,i_n}$ are indexed by $i_n \in 1, 2, \ldots, I_n$ for $1 \leq n \leq N$.

Throughtout this paper, the mathematical notation used by Kolda et al. [17] has been adopted. Table 2 summarize this notation. ~~Tensor algebra notation summary~~ ~~$\mathcal{A}$, $\mathbf{A}$, $\mathbf{a}$, a Tensor, matrix, vector and scalar respectively~~~~$\mathcal{A} \in \mathbb{R}^{I_1 \times \cdots \times I_N}$ N-order tensor of size $I_1 \times \cdots \times I_N$.~~ ~~$a_{i_1 \ldots i_N}$ An element of a tensor~~ ~~$\mathbf{a}_{:i_2 i_3}$, $\mathbf{a}_{i_1 : i_3}$, and $\mathbf{a}_{i_1 i_2 :}$ Column, row and tube fibers of a third order tensor~~~~$\mathbf{A}_{i_1 ::}$, $\mathbf{A}_{:i_2 :}$, $\mathbf{A}_{::i_3}$ Horizontal, lateral and frontal slices for a third order tensor~~ ~~$\mathbf{A}^{(n)}$, $\mathbf{a}^{(n)}$ A matrix/vector element from a sequence of matrices/vectors~~ ~~$\mathbf{A}_{(n)}$ Mode-n matricization of a tensor.~~ ~~$\mathbf{A}_{(n)} \in \mathbb{R}^{I_n \times \prod_{m \neq n} I_m}$~~ ~~$\mathcal{X} = \mathbf{a}^{(1)} \circ \cdots \circ \mathbf{a}^{(N)}$ Outer product of N vectors, where $x_{i_1 i_2 \ldots i_N} = a^{(1)}_{i_1} \ldots a^{(N)}_{i_N}$~~ ~~$\langle \mathcal{A}, \mathcal{B} \rangle$ Inner product of two tensors.~~ ~~$\mathcal{B} = \mathcal{A} \times_n \mathbf{U}$ n-mode product of tensor $\mathcal{A} \in \mathbb{R}^{I_1 \times \cdots \times I_N}$ by a matrix $\mathbf{U} \in \mathbb{R}^{I \times I_n}$ along axis n.~~

2.1. ~~Basic concepts~~

It is also necessary to introduce some tensor algebra operations and basic concepts used in later explanations. ~~These notations were taken textually from [17].~~

2.0.1. ~~Matricization~~

2.1. Matricization

The mode-n matricization is the process of reordering the elements of a tensor into a matrix along axis n and it is denoted as $\mathbf{A}_{(n)} \in \mathbb{R}^{I_n \times \prod_{m \neq n} I_m}$.

2.1.1. ~~Outer Product~~

~~The outer product of N vectors $\mathcal{X} = \mathbf{a}^{(1)} \circ \cdots \circ \mathbf{a}^{(N)}$ produces a tensor $\mathcal{X} \in \mathbb{R}^{I_1 \times \cdots \times I_N}$ where $\circ$ denotes the outer product and $\mathbf{a}^{(n)}$ denotes a vector in a sequence of N vectors and each element of the tensor is the product of the corresponding vector elements; i.e., $x_{i_1 i_2 \ldots i_N} = a^{(1)}_{i_1} \ldots a^{(N)}_{i_N}$.~~

2.1.1. ~~Inner Product~~

~~The~~

2.2. Inner Product

The inner product of two tensors $\mathcal{A}, \mathcal{B} \in \mathbb{R}^{I_1 \times \cdots \times I_N}$ is the sum of the products of their entries; i.e., $\langle \mathcal{A}, \mathcal{B} \rangle = \sum_{i_1=1}^{I_1} \cdots \sum_{i_N=1}^{I_N} a_{i_1 \ldots i_N} b_{i_1 \ldots i_N}$.

2.2.1. ~~N-Mode Product~~

2.3. N-Mode Product

It means the multiplication of a tensor $\mathcal{A} \in \mathbb{R}^{I_1 \times \cdots \times I_N}$ by a matrix $\mathbf{U} \in \mathbb{R}^{J \times I_n}$ or vector $\mathbf{u} \in \mathbb{R}^{I_n}$ in mode n; i.e., along axis n. It is represented by $\mathcal{B} = \mathcal{A} \times_n \mathbf{U}$, where $\mathcal{B} \in \mathbb{R}^{I_1 \times \cdots \times I_{n-1} \times J \times I_{n+1} \times \cdots \times I_N}$ [17].

2.3.1. ~~Rank-One Tensor~~

2.4. Rank-One Tensor

A tensor $\mathcal{X} \in \mathbb{R}^{I_1 \times \cdots \times I_N}$ is rank one if it can be written as the outer product of N vectors~~;~~, i.e., ~~$\mathcal{X} = \mathbf{a}^{(1)} \circ \cdots \circ \mathbf{a}^{(N)}$.~~

2.4.1. ~~Rank-R Tensor~~

~~The rank of a tensor rank($\mathcal{X}$) is the smallest number of components in a CPD~~

$$\mathcal{X} = \mathbf{a}^{(1)} \circ \cdots \circ \mathbf{a}^{(N)} \tag{1}$$

where $\circ$ denotes the outer product and $\mathbf{a}^{(n)}$ denotes a vector in a sequence of N vectors. Each element of the tensor is the product of the corresponding vector elements; i.e., ~~the smallest number of rank-one tensors that generate $\mathcal{X}$ as their sum [17].~~ $x_{i_1 i_2 \ldots i_N} = a^{(1)}_{i_1} \ldots a^{(N)}_{i_N}$.

2.4.1. N-Rank

The n-rank of a tensor $\mathcal{X} \in \mathbb{R}^{I_1 \times \cdots \times I_N}$ denoted $\text{rank}_n(\mathcal{X})$, is the column rank of $\mathbf{X}_{(n)}$; i.e., the dimension of the vector space spanned by the mode-n fibers. Hence, if $R_n \equiv \text{rank}_n(\mathcal{X})$ for $n = 1, \ldots, N$, we can say that $\mathcal{X}$ has a rank $-(R_1, \ldots, R_N)$ tensor [17].

Table 2. Tensor algebra notation summary

$\mathcal{A}$, $\mathbf{A}$, $\mathbf{a}$, a	Tensor, matrix, vector and scalar respectively
$\mathcal{A} \in \mathbb{R}^{I_1 \times \cdots \times I_N}$	N-order tensor of size $I_1 \times \cdots \times I_N$.
$a_{i_1, \ldots, i_N}$	An element of a tensor
$\mathbf{a}_{:i_2 i_3}$, $\mathbf{a}_{i_1 :i_3}$, and $\mathbf{a}_{i_1 i_2 :}$	Column, row and tube fibers of the third order tensor $\mathcal{A}$
$\mathbf{A}_{i_1 ::}$, $\mathbf{A}_{:i_2 :}$, $\mathbf{A}_{::i_3}$	Horizontal, lateral and frontal slices of the third order tensor $\mathcal{A}$
$\mathbf{A}^{(n)}$, $\mathbf{a}^{(n)}$	A matrix/vector element from a sequence of matrices/vectors
$\mathbf{A}_{(n)}$	Mode-n matricization of a tensor. $\mathbf{A}_{(n)} \in \mathbb{R}^{I_n \times \prod_{m \neq n} I_m}$
$\mathbf{a}^{(1)} \circ \cdots \circ \mathbf{a}^{(N)}$	Outer product of N vectors
$\langle \mathcal{A}, \mathcal{B} \rangle$	Inner product of two tensors.
$\mathcal{B} = \mathcal{A} \times_n \mathbf{U}$	n-mode product of tensor $\mathcal{A} \in \mathbb{R}^{I_1 \times \cdots \times I_N}$ by a matrix $\mathbf{U} \in \mathbb{R}^{J \times I_n}$ along axis n.

3. Tensor decompositions (TDs)

As an extension of the matrix-based singular value decomposition, two main specific tensor decompositions can be considered; Tucker Decomposition (TKD) [] and CANDECOMP/PARAFAC (CP) []. There are many other tensor decompositions; INDSCAL, PARAFAC2, CANDELINC, DEDICOM, PARATUCK2, among others [17]. Furthermore, there are also nonnegative variants of all of the above. With the aim of preserving particular characteristics of hyperspectral images for pixel-wise classification, this study is limited to use decompositions based on the Tucker model.

3.1. Tucker Decomposition (TKD)

The TKD [17], for the particular case of third-order tensors, can be formally formulated as follows [**?**]. Given a third-order data tensor $\mathcal{X} \in \mathbb{R}^{I_1 \times I_2 \times I_3}$ and three positive indices J_1, J_2 and J_3, find a core tensor $\mathcal{G} \in \mathbb{R}^{J_1 \times J_2 \times J_3}$ and three component matrices called factor matrices ~~$\mathbf{U}_1 \in \mathbb{R}^{I_1 \times J_1}$, $\mathbf{U}_2 \in \mathbb{R}^{I_2 \times J_2}$ and $\mathbf{U}_3 \in \mathbb{R}^{I_3 \times J_3}$~~ $\mathbf{U}^1 \in \mathbb{R}^{I_1 \times J_1}$, $\mathbf{U}^2 \in \mathbb{R}^{I_2 \times J_2}$ and $\mathbf{U}^3 \in \mathbb{R}^{I_3 \times J_3}$ which perform the following approximate decomposition:

$$\mathcal{X} = \mathcal{G} \times_1 \mathbf{U}^{(1)} \times_2 \mathbf{U}^{(2)} \times_3 \mathbf{U}^{(3)} + \mathcal{E} \tag{2}$$

where $\mathcal{E}$ denotes the approximation error tensor. The core tensor $\mathcal{G}$ preserves the level of interaction for each factor or projection matrix $\mathbf{U}^{(n)}$. The factor matrices are commonly considered orthogonal, but in Tucker models with non-negativity constraints, that is not necessarily imposed [**?**]. These matrices can be seen as the principal components in each mode [17] (see Figure 1). J_n represents the number of components in the decomposition; i.e., the rank $-$ (R_1, R_2, R_3).

We can also denote the TKD using the matricization approach and express it by

$$\mathbf{X}_{(1)} = \mathbf{U}^{(1)} \mathbf{G}_{(1)} (\mathbf{U}^{(3)} \otimes \mathbf{U}^{(2)})^T \tag{3a}$$

$$\mathbf{X}_{(2)} = \mathbf{U}^{(2)} \mathbf{G}_{(2)} (\mathbf{U}^{(3)} \otimes \mathbf{U}^{(1)})^T \tag{3b}$$

$$\mathbf{X}_{(3)} = \mathbf{U}^{(3)} \mathbf{G}_{(3)} (\mathbf{U}^{(2)} \otimes \mathbf{U}^{(1)})^T \tag{3c}$$

where $\otimes$ denotes the Kronecker product and $\mathbf{X}_{(n)}$ and $\mathbf{G}_{(n)}$ are the n-mode matricized versions of tensor $\mathcal{X}$ and $\mathcal{G}$ respectively.

Starting from (2), the reconstruction of an approximated tensor can be given by

$$\hat{\mathcal{X}} = \mathcal{G} \times_1 \mathbf{U}^{(1)} \times_2 \mathbf{U}^{(2)} \times_3 \mathbf{U}^{(3)} \tag{4}$$

where $\hat{\mathcal{X}}$ is the reconstructed tensor.

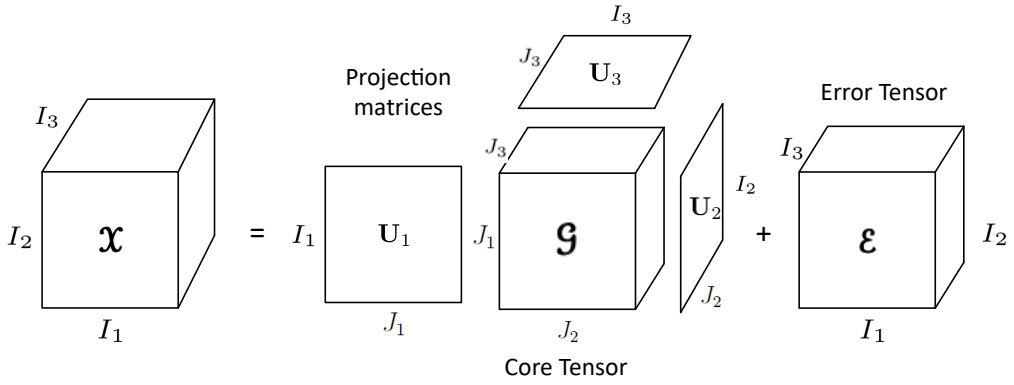

Figure 1. Tucker decomposition for a third-order tensor.

Then, we can acquire the core tensor $\mathcal{G}$ by the multilinear projection

$$\mathcal{G} = \mathcal{X} \times_1 \mathbf{U}^{(1)\mathrm{T}} \times_2 \mathbf{U}^{(2)\mathrm{T}} \times_3 \mathbf{U}^{(3)\mathrm{T}} \tag{5}$$

where $\mathbf{U}^{(n)\mathrm{T}}$ denotes the transpose matrix of $\mathbf{U}^{(n)}$ for $n = 1, \ldots, N$. The reconstruction error ξ can be computed as

$$\xi(\hat{\mathcal{X}}) = ||\mathcal{X} - \hat{\mathcal{X}}||_F^2 \tag{6}$$

and $||\cdot||_F$ represents the Frobenius norm. To compute the best rank approximation of a tensor, it ~~is required~~ can be used an iterative algorithm ~~. HOSVD, ALSand HOOI are algorithms commonly used in TKD~~ as ALS, HALS, HOOI after a HOSVD initialization [**?**].

HOOI initializes the factors matrices using HOSVD and assumes that othogonal matrices are known, so that the core tensor is obtained with (5). Then, it maximizes the cost function

$$\max_{\mathbf{U}^{(1)},\mathbf{U}^{(2)},\mathbf{U}^{(3)}} ||\mathcal{X} \times_1 \mathbf{U}^{(1)\mathrm{T}} \times_2 \mathbf{U}^{(2)\mathrm{T}} \times_3 \mathbf{U}^{(3)\mathrm{T}}||_F^2 \tag{7}$$

with $\mathbf{U}^{(n)}$ unknown. Fixing all factor matrices but one, tensor $\mathcal{X}$ can be projected onto the $\{R_1, \ldots, R_{n-1}, R_{n+1}, \ldots, R_N\}$-dimensional space as

$$\mathcal{W}^{(-n)} = \mathcal{X} \times_1 \mathbf{U}^{(1)\mathrm{T}} \cdots \times_{n-1} \mathbf{U}^{(n-1)\mathrm{T}} \times_{n+1} \mathbf{U}^{(n+1)\mathrm{T}} \cdots \times_N \mathbf{U}^{(N)\mathrm{T}} \tag{8}$$

and the orthogonal matrices can be estimated as an orthonormal basis for the dominant subspace of the projection by applying the standard matrix SVD for n-mode unfolded matrix $\mathcal{W}_{(n)}^{(-n)}$ for $n = 1, 2, 3$ [**?**].

3.1.1. Non-negative Tucker Decomposition (NTD)

The NTD is a ~~Tucker decomposition with nonegativity constraints, which~~ decomposition based on the Tucker model. It is develops a new tensor factorization method ~~[]. Thus, for~~ with nonegativity constraints []. For the third-order case, the NTD, as defined by Cichocky [15], can be formulated as follows. Given a third-order tensor $\mathcal{X} \in \mathbb{R}_+^{I_1 \times I_2 \times I_3}$ find a core tensor $\mathcal{G} \in \mathbb{R}_+^{I_1 \times I_2 \times I_3}$ and the factor matrices $\mathbf{U}_1 \in \mathbb{R}_+^{I_1 \times J_1}$, $\mathbf{U}_2 \in \mathbb{R}_+^{I_2 \times J_2}$ and $\mathbf{U}_3 \in \mathbb{R}_+^{I_3 \times J_3}$ which performs the approximation given in Eq. (2). ~~The TKD method is similarly followed for the NTD.~~

~~The HOOI algorithm can be applied for the particular case of third-order tensor . Furthermore, it can be slightly adjusted for preserving any input dimension and develop the decomposition in a specific order~~As well as for the TKD model, the best rank approximation of a nonnegative tensor can be computed by an iterative algotihm as HOOI, maximizing the cost function given in equation 7.

Algorithm 1 shows the HOOI algorithm for a NTD.

Algorithm 1: HOOI algorithm to compute a rank-$(R_1, \ldots, R_N)$ NTD for an Nth-order tensor $\mathcal{X} \in \mathbb{R}^{I_1 \times \cdots \times I_N}$.

Function `HOOI`$(\mathcal{X}, J_1, \ldots, J_N)$**:**
- initialize $\mathbf{U}^{(n)} \in \mathbb{R}^{I_n \times J_n}$ for $n = 1, \ldots, N$ using HOSVD or random
- **repeat**
  - **for** $n = 1, \ldots, N$ **do**
    - $\mathcal{W}^{(-n)} \leftarrow \mathcal{X} \times_{-n} \{\mathbf{U}^{\mathrm{T}}\}$
    - $\left[\mathbf{U}^{(n)}, \mathbf{\Sigma}^{(\mathbf{n})}, \mathbf{V}^{(n)}\right] \leftarrow \text{svds}(\mathcal{W}^{(-n)}_{(n)}, J_n, \text{'LM'})$
    - $\mathbf{U}^{(n)} \leftarrow \left[\mathbf{U}^{(n)}\right]_+$
  - **end**
- **until** *fit ceases to improve or maximum iterations exhausted*;
- $\mathcal{G} \leftarrow \mathcal{W}^{(-N)} \times_N \mathbf{U}^{(N)\mathrm{T}}$

Output: $\mathbf{U}^{(n)} \in \mathbb{R}_+^{I_n \times J_n}$, $\mathcal{G} \in \mathbb{R}_+^{J_1 \times J_2 \times \cdots J_N}$

4. Problem phenomenology

4.1. Spectral Imagery

Multi- or Hyper-spectral images are by nature multidimensional integer nonnegative arrays. A spectral image can be sorted and represented as a third-order tensor ~~$\mathcal{X} \in \mathbb{R}_+^{I_1 \times I_2 \times I_3}$, where~~ $\mathcal{X} \in \mathbb{N}^{I_1 \times I_2 \times I_3}$, where $\mathbb{N}$ denotes the space of natural numbers, $I_!$, I_2 and I_3 represent ~~its~~ the height, widht and spectral bands respectively. In RS image processing, spectral images are frequently used for classification of different material in a scene of interest. However, due to the low spatial resolution produced by the distance between the sensor an the target, spatial features are not sufficient to discern certain classes. That is why spectral resolution plays an important role in this type of task.

The separation into spectral bands allows perception of reflectance at different wavelengths. This helps to better characterize various materials, in order to simplify the process of discernment between classes. The effort to obtain these spectral features generates a greater amount of data, which increases the processing complexity. This is where the spectral decomposition task becomes relevant.

4.2. Problem Statement

~~Given a Spectral Image~~ Let $\mathcal{X} \in \mathbb{N}^{I_1 \times I_2 \times I_3}$ be a spectral image represented as a third-order tensor~~$\mathcal{X} \in \mathbb{R}^{I_1 \times I_2 \times I_3}$, and its corresponding pixelwise classification~~ , and $\mathbf{Y} \in \mathbb{N}^{I_1 \times I_2}$ its corresponding ground truth matrix ~~$\mathbf{Y} \in \mathbb{R}^{I_1 \times I_2}$~~ for a specific number of classes C~~, find, through Non-negative Tensor Decomposition,~~ . Find the best rank-(R_1, R_2, R_n) approximation and its ~~respective~~ core tensor $\mathcal{G} \in \mathbb{R}^{I_1 \times I_2 \times J_3}$, through Non-negative Tensor Decompositions. The rank of the decomposition $\text{rank}_n(\mathcal{X})$ is set as rank-(I_1, I_2, J_3), where ~~$R_1 = I_1, R_2 = I_2$ and $R_3 = J_3 << I_3$, to be the input~~ $J_3 < I_3$. This built the input space of a pixel-wise classification ~~Convolutional Neural Network~~ using CNNs and produce an output matrix $\hat{\mathbf{Y}}$ of predicted classes, achieving competitive performance metrics for pixel-wise classification while decreasing computational load in the classification process.

4.3. Mathematical Definition

We can mathematically define the problem statement described above as an optimization problem.

$$
\begin{aligned}
\min_{\mathcal{G},\mathbf{U}^{(1)},\mathbf{U}^{(2)},\mathbf{U}^{(3)}} \quad & ||\mathcal{X} - \mathcal{G} \times_1 \mathbf{U}^{(1)} \times_2 \mathbf{U}^{(2)} \times_3 \mathbf{U}^{(3)}||_F^2 \\
\text{subject to} \quad & \mathbf{U}^{(n)} \in \mathbb{R}_+^{I_n \times J_n} \quad \text{for} \quad n = 1,2,3 \quad \text{and} \quad \mathcal{G} \in \mathbb{R}_+^{J_1 \times J_2 \times J_3} \\
& J_1 = I_1, J_2 = I_2 \qquad \text{no compression in the spatial domain,} \\
& J_3 < I_3 \qquad \text{reduced spectral domain at the core tensor,} \\
& D(\mathcal{G}_{j_3}) - D(\mathcal{G}_{j_3+1}) < D_s \qquad \text{rank searching stop criterion}
\end{aligned}
\tag{9}
$$

5. Deep Convolutional Neural Networks (DCNNs)

CNNs are supervised feed-forward DL-ANNs for computer vision. The idea of applying a sort of convolution of the synaptic weights of a neural network through the input data yields to a preservation of spatial features, which alleviates the hard task of classification and in turn semantic segmentation. This type of ANN works under the same linear regression model as every machine learning (ML) algorithm. Since images are three dimensional arrays, we can use tensor algebra notation to describe the input of CNNs as a tensor $\mathcal{A} \in \mathbb{R}^{I_1 \times I_2 \times I_3}$, where I_1, I_2, and I_3 represent height, width, and depth of the third order array respectively; i.e., the spatial and spectral domain of an image. We can write generally the linear regression model used for ANNs as

$$\hat{\mathbf{y}} = \sigma\left(\mathbf{W}\mathbf{g} + \mathbf{b}\right)$$

where $\hat{\mathbf{y}}$ represents the output prediction of the network; σ denotes an activation function; $\mathbf{g}$ is the input dataset; $\mathbf{W}$ and $\mathbf{b}$ are the matrix of synaptic weights and the bias vector, respectively. These parameters are adjustable; i.e., their values are modified every iteration looking for convergence to minimize the loss in the prediction through optimization algorithms [32]. For simplicity, the bias vector can be ignored, assuming that matrix $\mathbf{W}$ will update until convergence independently of another parameter [32]. Considering that the input dataset to a CNN is a multidimensional array, we can represent and using tensor algebra notation as

$$\hat{\mathcal{Y}} = \sigma\left(\mathcal{W}\mathcal{G}\right)$$

where $\hat{\mathcal{Y}}$ represents the prediction output tensor of the ANN (in our case, a second order tensor or matrix $\hat{\mathbf{Y}}$), $\mathcal{G}$ is the input dataset, and $\mathcal{W}$ is a $K_1 \times K_2 \times F_1$ tensor called filter or kernel with the adaptable synaptic weights. Different to conventional ANN, in CNNs, $\mathcal{W}$ is a shiftable square tensor is much smaller in height and width than the input data, i.e., $K_1 = K_2$ and $K_s << I_s$ for $s = 1,2$; F_1 denotes the number of input channels; i.e., $F_1 = I_3$. For hidden layers, instead of the prediction tensor $\hat{\mathcal{Y}}$, the output is a matrix called activation map $\mathbf{M} \in \mathbb{R}^{I_1 \times I_2}$, which preserves features from the original data in each domain. Actually, it is necessary to use much kernels $\mathcal{W}^{(f_2)}$ as activation maps, with different initialization values to preserve diverse features of the image. Hence, we can also define activation maps as a tensor $\mathcal{M} \in \mathbb{R}^{I_1 \times I_2 \times F_2}$ where F_2 denotes the number of activation maps produced by each filter (see Figure **??**). Kernels are displaced through the whole input image as a discrete convolution operation. Then, each element of the output activation map $m_{i_1 i_2 f_2}$ is computed by the summary of the Hadamard product of kernel $\mathcal{W}^{(f_2)}$ and a subtensor from the input tensor $\mathcal{G}$ centered in position (i, j) and with same dimensions of $\mathcal{W}$, as follows

$$m_{i_1 i_2 f_2} = \sigma\left[\sum_{k_1=1}^{K_1}\sum_{k_2=1}^{K_2}\sum_{f_1=1}^{F_1} w_{k_1,k_2,f_1} g_{i_1+k_1-o_1,i_2+k_2-o_2,f_1}\right]$$

where $m_{i_1 i_2 f_2}$ denotes the value of the output activation map f_2 at position i_1, i_2; σ represents the activation function; and o_1 and o_2 are offsets in spatial dimensions which depend on the kernel size, and equal $\frac{K_1+1}{2}$ and $\frac{K_2+1}{2}$ respectively (see Figure **??**).Convolutional layer with a $K_1 \times K_2 \times F_1 \times F_2$ kernel. Input channels F_1 must equal the spectral bands I_3. To preserve original dimensions at the output, zero padding is needed [18]. Output dimensions also depend on stride $S = 1$ to consider every piece of pixel information and to preserve original dimensions.

An ANN is trained by using iterative gradient-based optimizers, such as Stochastic gradient descent, Momentum, RMSprop, and Adam [32]. This drive the cost function $L(\boldsymbol{\mathcal{W}})$ to a very low value by updating the synaptic weights $\boldsymbol{\mathcal{W}}$. We can compute the cost function by any function that measures the difference between the training data and the prediction, such as Euclidean distance or cross-entropy [10]. Besides, the same function is used to measure the performance of the model during testing and validation. In order to avoid overfitting [32], the total cost function used to train an ANN combines one of the cost functions mentioned before, plus a regularization term.

$$J(\boldsymbol{\mathcal{W}}) = L(\boldsymbol{\mathcal{W}}) + R(\boldsymbol{\mathcal{W}}),$$

where $J(\boldsymbol{\mathcal{W}})$ denotes the total cost function and $R(\boldsymbol{\mathcal{W}})$ represents a regularization function. Then, we can decrease $J(\boldsymbol{\mathcal{W}})$ by updating the synaptic weights in the direction of the negative gradient. This is known as the method of steepest descent or gradient descent.

$$\boldsymbol{\mathcal{W}}' = \boldsymbol{\mathcal{W}} - \phi \nabla_{\boldsymbol{\mathcal{W}}} J(\boldsymbol{\mathcal{W}}),$$

where $\boldsymbol{\mathcal{W}}'$ represents the synaptic weights tensor in next iteration during training, ϕ denotes the learning rate parameter, and $\nabla_{\boldsymbol{\mathcal{W}}} J(\boldsymbol{\mathcal{W}})$ the cost function gradient. Gradient descent converges when every element of the gradient is zero, or in practice, very close to zero [10].

CNNs has been successfully used in many image classification frameworks. This variation in architecture from other typical ANN models yields the network to learn spatial and spectral features, which are highly profitable for image classification. Besides, FCNs, constructed with only convolutional layers are able to classify each element of the input image; i.e., they yield pixel-wise classification, or in other words, semantic segmentation.

5. Methodology

The following subsections described the methodology followed for the framework propose in this work. We can summarize the big picture in three steps: the HSI modeling, the tensor decomposition, the classifier and the decision making.

5.1. Tensor modeling

Consider an input dataset $\boldsymbol{\mathcal{X}} \in \mathbb{N}^{I_1 \times I_2 \times I_3}$ with $I_1 \times I_2 \times I_3$ samples in the space of the natural numbers $\mathbb{N}$, where a fiber $\mathbf{x}_{i_1 i_2}$ represents the spectra or endmember of pixel $i_1 i_2$ and can be represented by the Linear Mixing Model (LMM) as follows

$$\mathbf{x}_{i_1 i_2} = \sum_{c=1}^{C} (\alpha_{i_1 i_2 c} \mathbf{m}_c + \boldsymbol{\eta}) \tag{10}$$

where α_c is the contribution of material c at pixel $i_1 i_2$, $\mathbf{m}_c$ denotes the endmember of a specific material c, and $\boldsymbol{\eta}$ represents an additive noise vector. The abundance vectors $\boldsymbol{\alpha}_{i_1 i_2}$ must always satisfy two constraints, i) the non-negativity, $\alpha_{i_1 i_2 c} \geq 0$ for all $c = 1, \ldots, C$, and ii) the sum-to-one restriction, $\sum_{c=1}^{C} \alpha_{i_1 i_2 c} = 1$. Figure 2a shows the spectral signatures for the Indian Pines dataset.

5.2. Tensor factorization

Consider $\mathbf{Y} \in \mathbb{C}^{I_1 \times I_2}$ as the matrix of actual classes corresponding to our dataset $\mathcal{X}$, and $\hat{\mathbf{Y}} \in \mathbb{C}^{I_1 \times I_2}$ as the prediction matrix, where $\mathbb{C}$ defines the set of C different classes. In order to reduce data dimensionality of the input dataset $\mathcal{X}$ while keeping classifier performance, we propose to use the restricted NTD denoted as $\mathcal{T}$, producing a core tensor $\mathcal{G} \in \mathbb{R}^{I_1 \times I_2 \times J_3}$ and n factors matrices $\mathbf{U}^{(n)} \in \mathbb{R}^{I_n \times J_n}$, expressed as

$$\mathcal{X} \xrightarrow{\mathcal{T}} (\mathcal{G}, \mathbf{U}^{(n)}) \tag{11}$$

where the decomposition is restricted to to preserve the spatial domain and to be only in the 3rd-mode by the Tucker1 model

$$\mathcal{X} = \mathcal{G} \times_1 \mathbf{I} \times_2 \mathbf{I} \times_3 \mathbf{U}^{(3)} \tag{12}$$

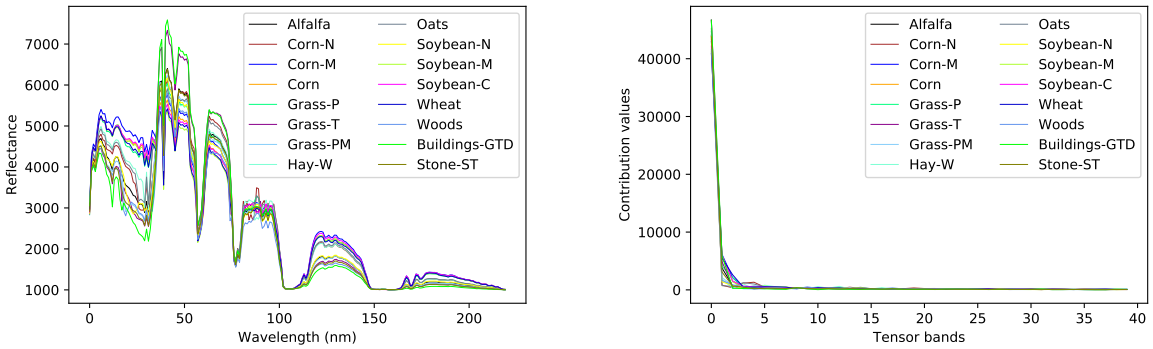

(a) **(b)**

Figure 2. Behavior of the 16 classes of the Indian Pines dataset, a) in the spectral domain (spectral signatures) and b) in the the tensor bands domain.

Hence, each fiber $\mathbf{x}_{i_1 i_2}$ of the core tensor takes a new representation in the tensor bands domain and can be mathematically defined as follows

$$\mathbf{g}_{i_1 i_2} = \sum_{c=1}^{C} (\beta_{i_1 i_2 c} \mathbf{s}_c + \eta) \tag{13}$$

where β_c is the contribution of material c at pixel $i_1 i_2$ and $\mathbf{s}_c$ denotes the endmember of a specific material c. We can see in Figure 2b the new tensor bands values for each class.

We also propose a variant of the NTD that does an integer decomposition, i. e., the Integer Non-negative Tucker decomposition (INTD). The INTD follows the same Tucker model described in Section 3.1. It considers the additional restriction of decomposing a tensor in the set of the natural numbers.

5.3. Classifier

The tensor decompostions ~~generates acore tensor~~based on the Tucker1 model produce a core tensor, where the first tensor bands provide ~~the most of the information~~ a signature enough to differentiate the classes of interest ~~from~~ of the input dataset. Then, the core tensor $\mathcal{G} \in \mathbb{N}^{I_1 \times I_2 \times J_3}$, with $J_3 < I_3$, and its corresponding ground truth $\mathbf{Y}$ form the input tuple of the classifier Θ, which produce a predicted label for each element of the input, i.e.,

$$(\mathcal{G}, \mathbf{Y}) \xrightarrow{\Theta} \hat{\mathbf{Y}} \tag{14}$$

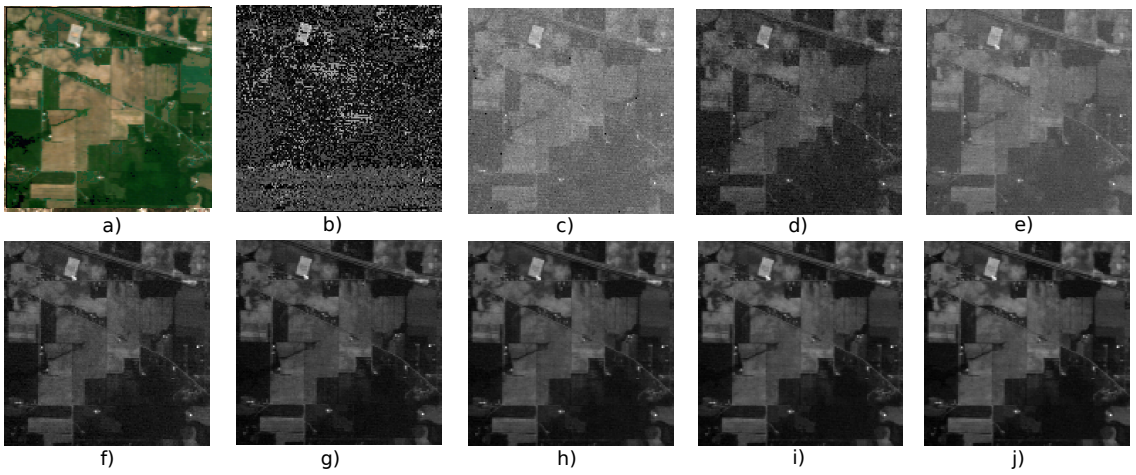

Figure 3. Indian Pines dataset a) True color image b) - j) 1st to 9th spectral band.

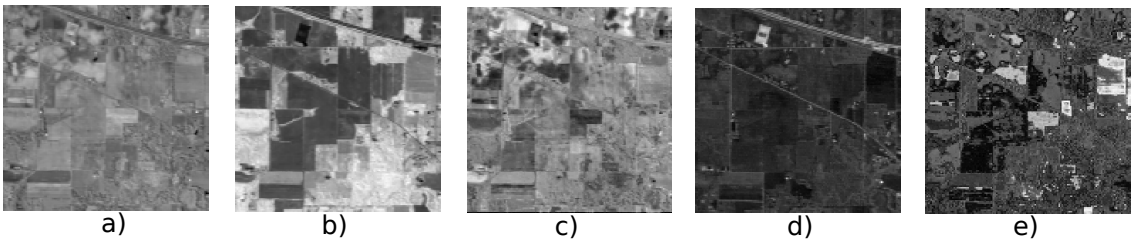

Figure 4. TKD tensor bands of the Indian Pines dataset a) - e) 1st to 5th tensor band.

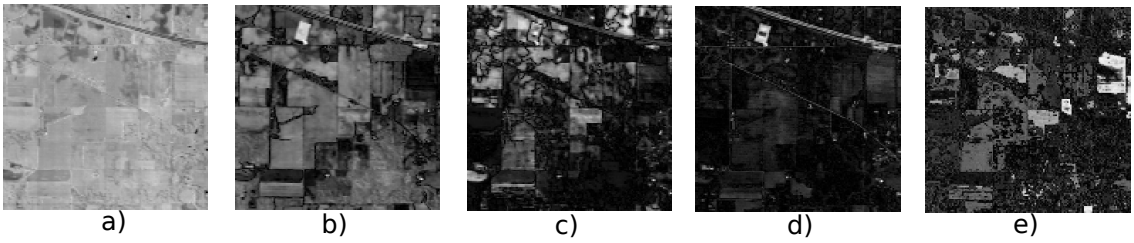

Figure 5. NTD tensor bands of the Indian Pines dataset a) - e) 1st to 5th tensor band.

The performance of our classification model can be measured by the cross-entropy loss, whose output is a probability value. The cross-entropy loss increases as the predicted probability diverges from the actual label and it is computed as

$$J(\mathcal{W}) = -\mathbb{E}_{\mathcal{G},\mathbf{Y}\sim\hat{p}} \log p(\mathbf{Y}|\mathcal{G}) \tag{15}$$

where $J(\mathcal{G})$ represents the loss function. For a multiclass probability distribution, the cross entropy cost function can be written as

$$H(y,p) = -\sum_{c=1}^{C} y_c \log(p_c) \tag{16}$$

where $H(y,p)$ denotes the cross entropy of targets y with a probability p.

We use the softmax function as the output of our classifier, to represent the probability distribution over C different classes. Formally, the softmax function is given by

$$\delta(\mathbf{z})_c = \frac{e^{z_c}}{\sum_{l=1}^{L} e^{z_l}} \tag{17}$$

where $\delta(\mathbf{z})_c$ denotes the softmax function of vector $\mathbf{z}$, which is each 3rd-mode fiber of the activation maps at the last convolutional layer. Hence, the softmax function produces a normalized probability distribution for every input pixel, which can be seen as the contribution parameter in the LMM Eq. 10.

In this paper, we aim to feed supervised classifiers, based on 3D-CNN, with a lower dimensionality tensor than the original dataset. This has three particular motivations: 1) to avoid overfitting the DCNN, 2) to reduce the computational complexity, and 3) keep the classifier performance while reducing the execution time. Figure 6 shows the big picture of the framework proposed.

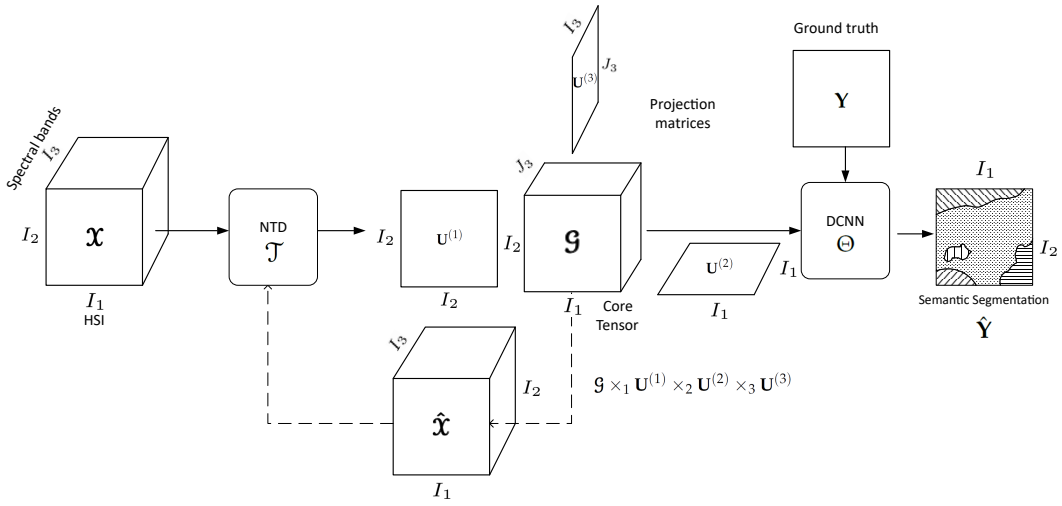

Figure 6. Big picture of the framework proposed.

5.4. Decomposition analysis

Our proposed framework faces two main challenges. The first is the selection of the decomposition method. We are looking for ~~the best~~ a better representation of the input dataset for a 3D-CNN, so, we limit the set of methods to those that produce a decomposition tensor with the same structure as the input tensor. TKD, NTD and the INTD proposed generate a core tensor with the desired properties.

The second challenge is the search for the rank $-(J_1, J_2, J_3)$. As we want to preserve the spatial domain $J_1 = I_1$ and $J_2 = I_2$, but J_3 has to be selected so that the performance of the classifier does not decrease considerably. Both decisions are made under a criterion under the probabilistic point of view.

The Kullback-Leibler divergence is a metric for quantifying the difference between the probability distributions of the original MSI X and the core tensor G as

$$D_{KL}(X\|G) = \sum_{i=1}^{I} p_i(x) \log \frac{p_i(x)}{g_i(x)} \tag{18}$$

where $D_{KL}(X\|G)$ represents the KL divergence of the two probability distributions. Figure 7a shows the results of this metric for the three decomposition used in this work.

Besides, a symetric version of the KL divergenge is used, the Jensen Shanon divergence. This is another method of measuring the similarity between two probability distributions. Defining $M = \frac{X+G}{2}$, we can write the JS divergence as

$$D_{JS}(X\|G) = \frac{1}{2} D_{KL}(X\|M) + \frac{1}{2} D_{KL}(G\|M) \tag{19}$$

where $D_{JS}(X\|G)$ represents the JS divergence of the probability distributions X and G. Figure 7b shows the JS divergence for the TKD, NTD and INTD.

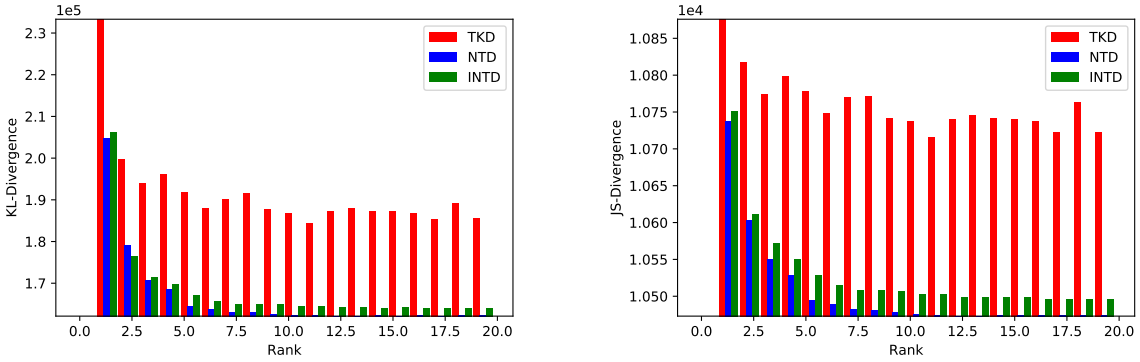

(a) **(b)**

Figure 7. Divergences between the input dataset and the core tensor generated by TKD, NTD and INTD, a) KL-divergence and b) JS-divergence.

6. Experimental Results

6.1. Input Data

For this work, we chose three of the most popular multi- and hyperspectral dataset for classification.

6.1.1. Sentinel-2

This dataset ~~developed~~ propose by Lopez et al. [**?**] is composed of RS Sentinel-2 scenarios from central Europe. It has 100 scenarios for the training space and 10 scenarios for testing, all of them with 128×128 pixels with spatial resolution of $20m^2$ and 9 spectral bands in the range $490 - 2190nm$. The labels are semi-manually asigned for five classes of interest: vegetation, soil, water, clouds and shadows. Data are available in the link Sentinel-2 Dataset.

Table 3. Average of contribution per class in Sentinel-2 dataset.

Class	Dataset ~~(%)~~	Train ~~(%)~~	Test~~(%)~~
Soil	~~23.58~~ 425,147	~~22.87~~ 374,792	~~30.73~~ 50,355
Shadow	~~2.52~~ 45,418	~~2.58~~ 42,281	~~1.91~~ 3,137
Cloud	~~13.87~~ 250,020	~~14.37~~ 235,546	~~8.83~~ 14,474
Water	~~12.13~~ 218,620	~~11.93~~ 195,512	~~14.10~~ 23,108
Vegetation	~~47.88~~ 863,035	~~48.23~~ 790,269	~~44.41~~ 72,766

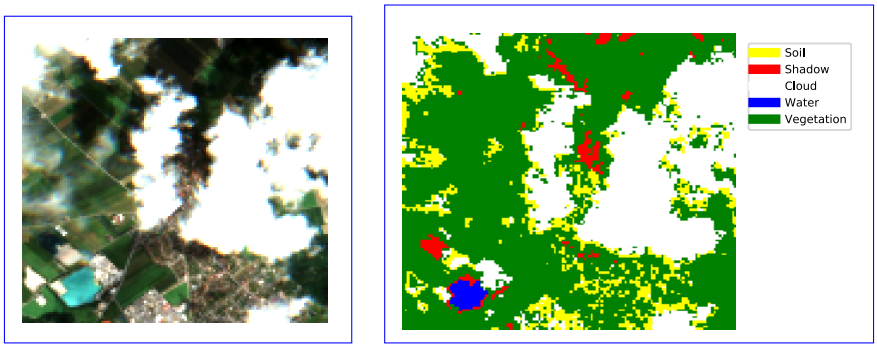

(a) **(b)**

Figure 8. Sentinel dataset, a) True color and b) Ground truth.

6.1.2. Indian Pines

This dataset is a scene produced by AVIRIS in North-western Indiana and consists of 145×145 pixels and 224 spectral bands in the wavelength range 0.4˜$2.5\mu m$. The Indian Pines scene contains two-thirds agriculture, and one-third forest or other natural perennial vegetation. There are two major dual lane highways, a rail line, as well as some low density housing, other built structures, and smaller roads. Since the scene is taken in June some of the crops present, corn, soybeans, are in early stages of growth with less than 5% coverage. The ground truth available is designated into sixteen classes and is not all mutually exclusive. Indian Pines data are available at Indian Pines dataset. Figure 9 shows the true color image of Salinas dataset, as well as the ground truth with each of its corresponding classes and Table 4 the number of samples for each class.

Table 4. Average of contribution per class in Indian Pines dataset.

Class	Samples
Alfalfa	46
Corn-notill	1428
Corn-mintill	830
Corn	237
Grass-pasture	483
Grass-tress	730
Grass-pasture-mowed	28
Hay-windrowed	478
Oats	20
Soybean-notill	972
Soybean-mintill	2455
Soybean-clean	593
Wheat	205
Woods	1265
Building-Grass-Trees-Drives	386
Stone-Steel-Towers	93

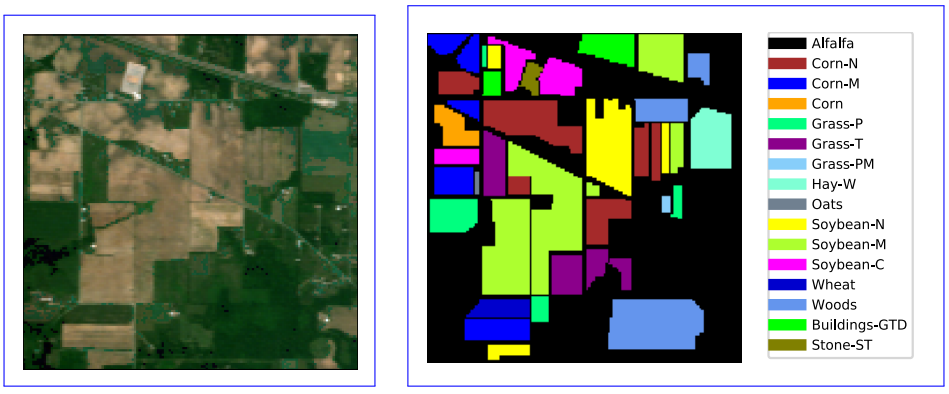

(a) **(b)**

Figure 9. Indian Pines dataset, a) True color and b) Ground truth.

6.1.3. Salinas

This scene was collected by the AVIRIS sensor over Salinas Valley, California. It has 512×217 pixels with spatial resolution $3.7m$, and 224 spectral bands. It includes vegetables, bare soils, and vineyard fields. Salinas groundtruth contains 16 classes ~~.~~ shows in table 5. Salinas data are available at Salinas dataset. Figure 10 shows the true color image of the Salinas dataset, as well as the ground truth labeled with each of its corresponding classes and Table 5 the number of samples for each class.

Table 5. Average of contribution per class in Salinas dataset.

Class	Samples
Brocoli-green-weeds-1	2009
Brocoli-green-weeds-2	3726
Fallow	1976
Fallow-rough-plow	1394
Fallow-smooth	2678
Stubble	3959
Celery	3579
Grapes-untrained	11271
Soil-vinyard-develop	6203
Corn-senesced-green-weeds	3278
Lettuce-romaine-4wk	1068
Lettuce-romaine-5wk	1927
Lettuce-romaine-6wk	916
Lettuce-romaine-7wk	1070
Vinyard-untrained	7268
Vinyard-vertical-trellis	1807

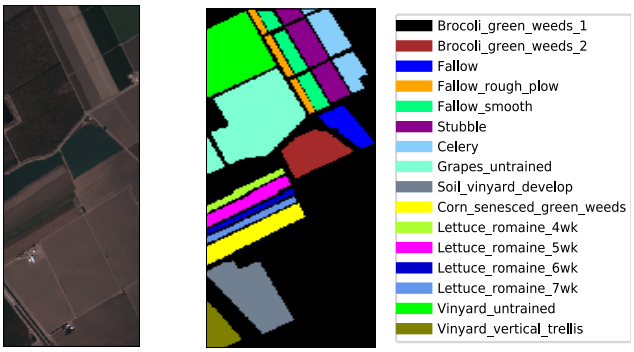

(a) **(b)**

Figure 10. Salinas dataset, a) True color and b) Ground truth.

6.1.4. Pavia University

This scene was collected by the ROSIS sensor over Pavia University, nothern Italy. It has 610×340 pixels with spatial resolution $1.3m$. and 103 spectral bands. Pavia groundtruth contains 9 classes, some of them described in table 6. Pavia University data are available at Pavia University dataset. Figure 11 shows the true color image of the Pavia dataset, as well as the ground truth labeled with each of its corresponding classes.

Table 6. Average of contribution per class in Pavia dataset.

Class	Samples
Asphalt	6631
Meadows	18649
Gravel	2099
Trees	3064
Painted metal sheets	1345
Bare Soil	5029
Bitumen	1330
Self-Blocking Bricks	3682
Shadows	947

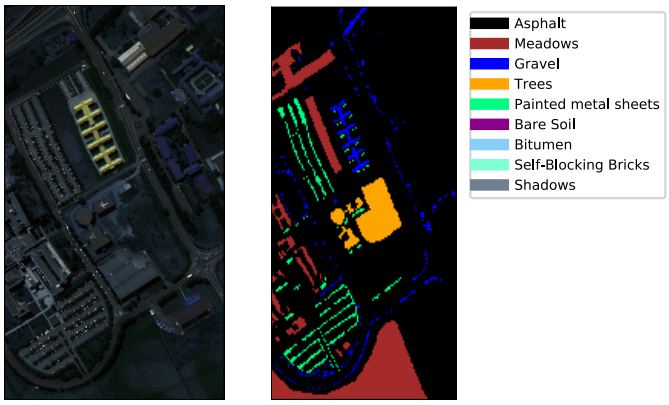

(a) **(b)**

Figure 11. Pavia dataset, a) True color and b) Ground truth.

In the following table 7 it is summarized the datasets used in this work as well as their spatial and spectral characteristics, the number of classes and their samples.

Table 7. Summary of the different dataset used for experiments in this work.

Dataset	Spatial dimensions	Bands	Classes	Samples
Sentinel-2 CNNMSI	128×128	9	5	16,~~220,160~~ 384
Indian Pines	145×145	~~224~~ 220	16	~~4,709,600~~ 21,025
Salinas	512×217	224	16	~~24,887,296~~ 111,104
Pavia University	610×340	103	9	207,400

6.2. ~~Metrics~~CNN Specifications

The model used to evaluate the framework proposed in this work is Segnet []. The strategie of cross-validation was used to set the hyperparameters of the CNN getting the following

- learning rate: 1×10^{-3}
- epochs: 100
- optimizer: Adam []
- initialization: Xavier []
- kernel dimensions: 3×3
- Activation Function: ReLU / Softmax

6.2.1. Computational Specifications

The software and hardaware tools used to run the framework proposed are summarized as follows

- Platform: Python 3.7
- AI Framework: Tensorflow 1.13
- GPU: NVIDIA GeForce GTX 1050 Ti
- Processor: Intel core i7
- RAM: 8GB
- SSD: 128GB / HDD: 1TB

6.3. Algorithms metrics

6.3.1. Relative Mean Square Error (rMSE)

~~In order to~~ To compute the reconstruction error of any decomposition, it can be used the relative Mean Square Error, given by

$$rMSE\left(\hat{\mathbf{x}}\right) = \frac{1}{Q}\sum_{q=1}^{Q}\frac{\left\|\hat{\mathbf{x}}_q - \mathbf{x}_q\right\|_F^2}{\left\|\mathbf{x}_q\right\|_F^2}, \tag{20}$$

where $\mathcal{X}_q$ represents the q-th MSI from a dataset with Q MSIs and $\hat{\mathcal{X}}_q$ its corresponding reconstruction computed by (4).

6.3.2. Loss

To quantify the convergence of the ~~tensor $\mathcal{X}$ for the implementation of HOOI, the rMSE was used :~~ iterative process in a supervised classification algorithm, it can be used a metric of difference between the lables $\mathbf{Y}$ and its corresponding prediction $\hat{\mathbf{Y}}$ as

$$rMSEMSE(\hat{\mathbf{Y}}) = \frac{1}{Q}\sum_{q=1}^{Q}\frac{\left\|\hat{\mathcal{X}}_q - \mathcal{X}_q\right\|_F^2}{\left\|\mathcal{X}_q\right\|_F^2}, \left\|\hat{\mathbf{Y}}-\mathbf{Y}\right\|_F^2 \tag{21}$$

where $\mathcal{X}_q$ represents the q-th CNNMSI from our dataset with Q MSIs and $\hat{\mathcal{X}}_q$ its corresponding reconstruction computed by (4).

6.4. *Evaluation metrics*

6.4.1. Cohen's Kappa Coefficient

Cohen's kappa coefficient is a very robust metric used to measure reliability of multi-class and imbalanced class classification algorithms []. It is computed by

$$\kappa = \frac{\rho_o - \rho_e}{1 - \rho_e} \tag{22}$$

where ρ_o is the observed agrrement, and ρ_e is the expected agreement. This metric will always produce values less than or equal to 1, where 1 means perfect agreement. Negative values indicate no agreement. i.e., futile classification.

6.4.2. Pixel Accuracy (PA)

We used the PA metric to compute a ratio between the amount of correctly classified pixels and the total number of pixels as follows. Given a confusion matrix relating the True Positive (TP), True Negatives (TN), False Positives (FP) and False Negatives (FN), the PA is computed by

$$PA = \frac{\sum_{c=1}^{C}\tau_{cc}}{\sum_{c=1}^{C}\sum_{d=1}^{C}\tau_{cd}} = \frac{TP+TN}{TP+TN+FP+FN} \tag{23}$$

where c is the number of class for $c = 1,\ldots,C$ and τ_{cc} is the amount of pixels of class c correctly assigned to class c i.e., TP and TN, and τ_{cd} is the amount of pixels of class c inferred to belong to class d. Despite this metric is wide used, it is not a totally fair metric for imbalanced classes. In this work we used this metric with comparison purposes. However, we also used metrics more in line with multi class classification tasks.

6.4.3. Precision

Another metric used in this work as a performance evaluation metric in multiclass classification is precision. This is a metric that measures the percentage of pixels from class c correctly classified. It is computed with the following equation

$$\Psi_c = \frac{\tau_{cc}}{\sum_{d=1}^{C}\tau_{cd}} = \frac{TP}{TP+FP} \tag{24}$$

where Ψ_c denotes the precision of class c, which is the number of TP divided by the TP plus FP.

6.4.4. Recall or Sensitivity

Recall, or also known as sensitivity is a metric that indicates the proportion of pixels classified as class c that actually belong to class c. It is computed with the following equation

$$v_c = \frac{\tau_{cc}}{\sum_{d=1}^{C} \tau_{dc}} = \frac{TP}{TP + FN} \tag{25}$$

where v_c denotes the recall of class c for $c = 1, \ldots, C$.

6.4.5. F1 Score

In order to summarize precision and recall in one only metric, we use the F1 score, which is computed by

$$F1 = \frac{2\Psi v}{\Psi + \Upsilon} \frac{2\Psi v}{\Psi + v} \tag{26}$$

This metric provides a very appropriate measure of multiclass classification for imbalanced dataset.

7. Discussion and Comparison

8. ~~Conclusions~~

7.1. ~~Figures, Tables and Schemes~~

~~Original Sentinel-2 spectral bands, a) True color image, b) to j) 1st to 9th spectral band respectively. Tensor bands from the Tucker Decomposition, a) to i) 1st to 9th band respectively. Tensor bands from the Non-negatice Tucker Decomposition, a) to i) 1st to 9th band respectively. Original Sentinel-2 spectral bands. Tucker Decomposition Tensor bands. Nonnegative Tucker Decomposition Tensor bands. Original Sentinel-2 spectral bands. Tucker Decomposition Tensor bands. Nonnegative Tucker Decomposition Tensor bands.~~

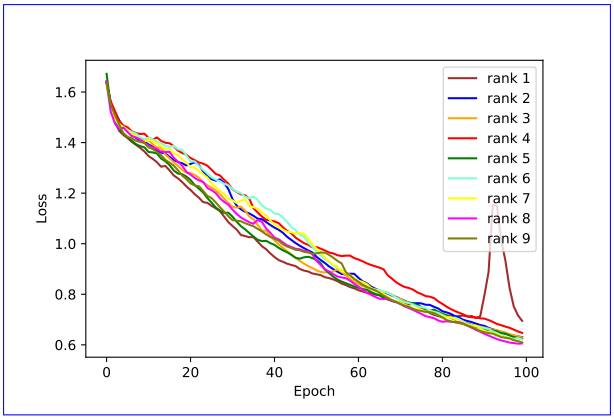

Figure 12. ~~Indian Pines Spectral Signatures a) Original, b)~~ Loss function of the CNN after NTD ~~and c) TKD~~for rank $J_3 = 1to9$.

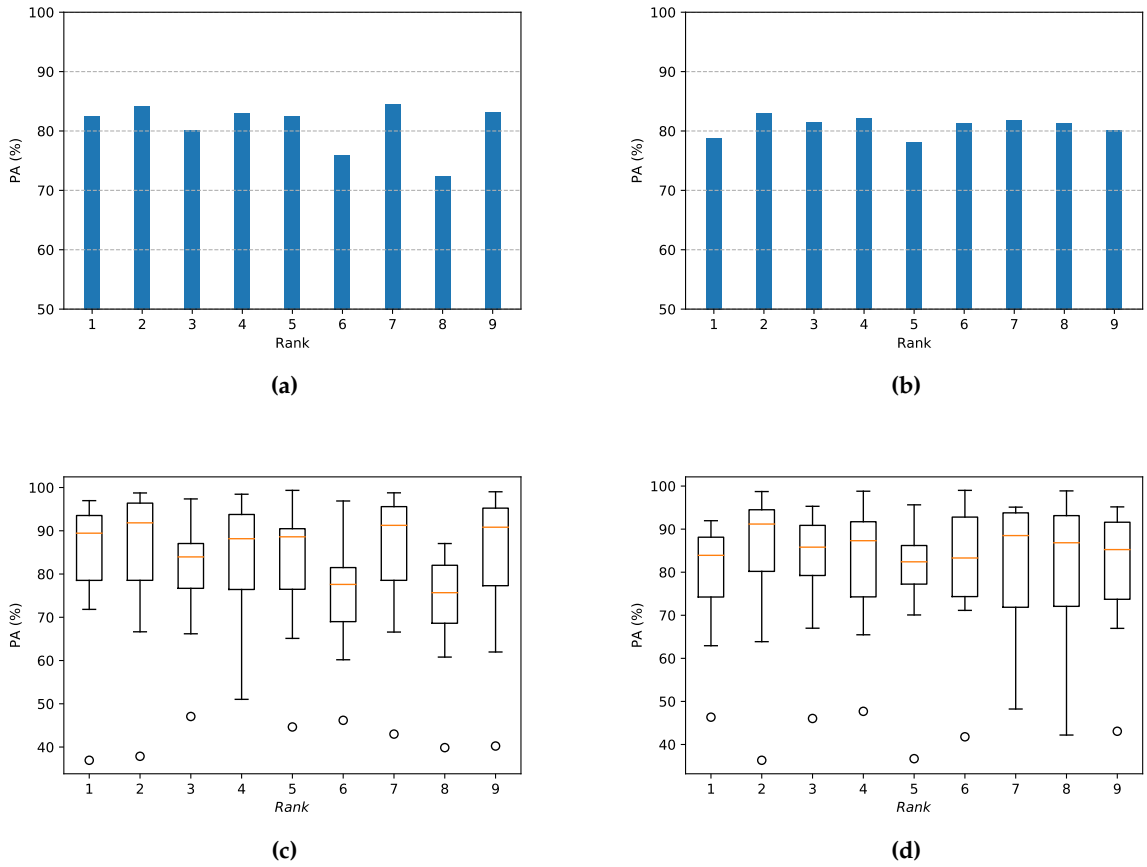

Figure 13. Pixel accuracy vs Rank results a) Comparative bar plot NTKD and TKD, b) Comparative bar plot NTKD and TKD c) Box and whiskers plot for NTKD, and d) Box and whiskers plot for TKD

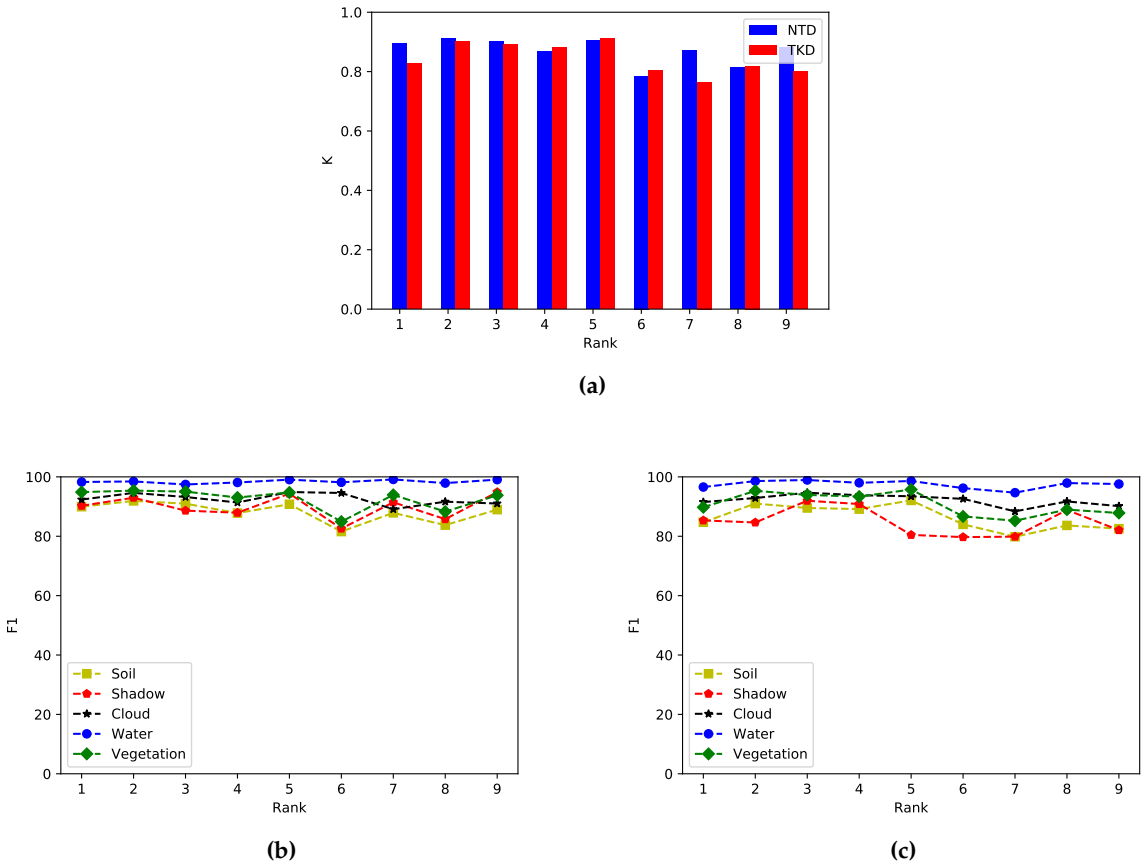

Figure 14. Performance evaluation metrics. a) Kappa score comparison NTD vs TKD, b) F1 for NTD and c) F1 for TKD

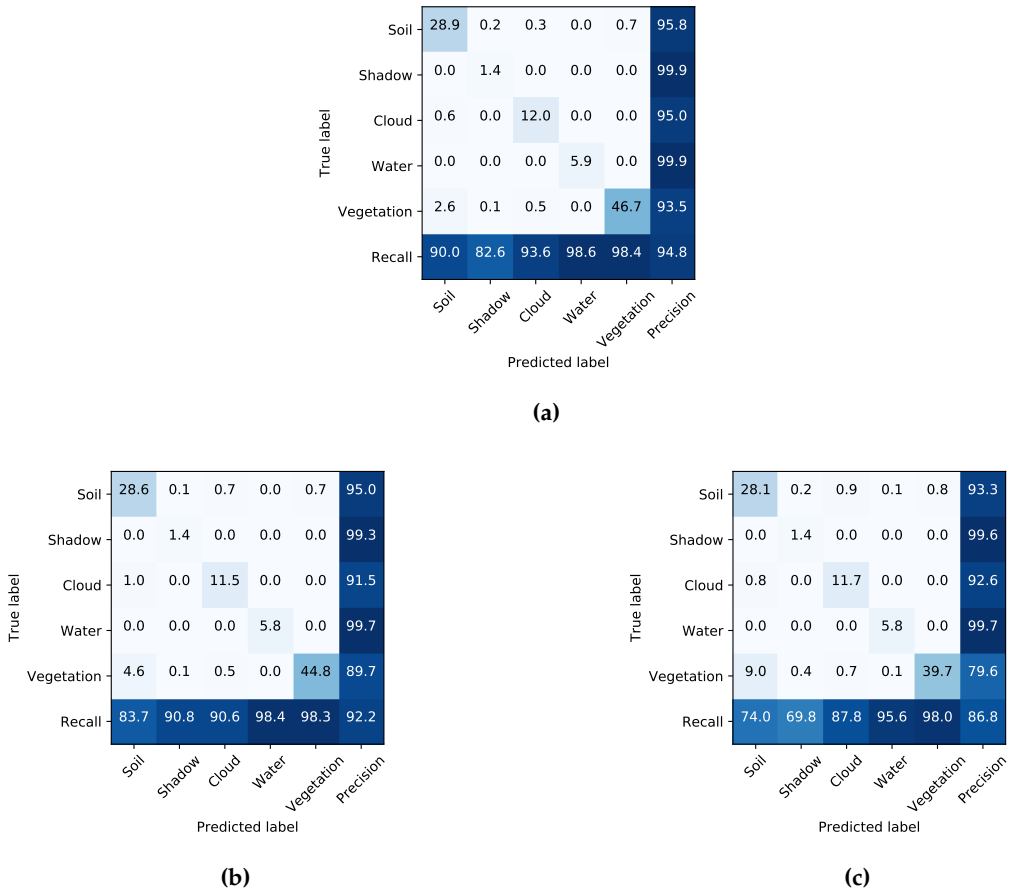

Figure 15. Confusion matrix for a) Sentinel-2 original dataset, b) NTD, c) TKD.

8. Conclusions

Author Contributions: Conceptualization, J.L.; formal analysis, D.T.; investigation, J.L.; methodology, J.L., D.T., and C.A.; resources, C.A.; software, J.L.; supervision, D.T. and C.A.; validation, D.T. and C.A.; writing—original draft, J.L. and D.T.

Funding: This work was supported by the National Council of Science and Technology CONACYT of Mexico under grant XXXXXXX.

Acknowledgments:

Conflicts of Interest: The authors declare no conflict of interest.

Abbreviations

The following abbreviations are used in this manuscript:

ANN	Artificial Neural Network
CNN	Convolutional neural network
CPD	Canonical Polyadic Decomposition
DL	Deep Learning
FCN	Fully Convolutional Network
HOOI	Higher-Order Orthogonal Iteration
HOSVD	Higher-Order Singular Value Decomposition

References

1. Tempfli, K.; Huurneman, G.; Bakker, W.; Janssen, L.; Feringa, W.; Gieske, A.; Grabmaier, K.; Hecker, C.; Horn, J.; Kerle, N.; et al. *Principles of Remote Sensing: An Introductory Textbook*, 4th ed.; ITC: Geneva, Switzerland, 2009.
2. He, Z.; Hu, J.; Wang, Y. Low-rank tensor learning for classification of hyperspectral image with limited labeled sample. *IEEE Signal Process.* **2017**, *145*, 12–25.
3. Richards, A.; Xiuping, J.J. Band selection in sentinel-2 satellite for agriculture applications. In *Remote Sensing Digital Image Analysis*, 4th ed.; Springer-Verlag: Berlin, Germany, 2006.
4. Zhang, T.; Su, J.; Liu, C.; Chen, W.; Liu, H.; Liu, G. Band selection in sentinel-2 satellite for agriculture applications. In Proceedings of the 23rd International Conference on Automation & Computing, University of Huddersfield, Huddersfield, UK, 7–8 September 2017.
5. Xie, Y.; Zhao, X.; Li, L.; Wang, H. Calculating NDVI for Landsat7-ETM data after atmospheric correction using 6S model: A case study in Zhangye city, China. In Proceedings of the 18th International Conference on Geoinformatics, Beijing, China, 18–20 June 2010.
6. Gao, B. NDWI—A normalized difference water index for remote sensing of vegetation liquid water from space. *Remote Sens. Environ.* **1996**, *58*, 1–6.
7. Ham, J.; Chen, Y.; Crawford, M.; Ghosh, J. Investigation of the random forest framework for classification of hyperspectral data. *IEEE Trans. Geosci. Remote Sens.* **2005**, *43*, 492–501.
8. Hearst, Marti A. Support Vector Machines. *IEEE Intell. Syst. J.* **1998**, *13*, 18–28.
9. Huang, X.; Zhang, L. An SVM Ensemble Approach Combining Spectral, Structural, and Semantic Features for the Classification of High-Resolution Remotely Sensed Imagery. *IEEE Trans. Geosci. Remote Sens.* **2013**, *51*, 257–272.
10. Delalieux, S.; Somers, B.; Haest, B.; Spanhove, T.; Vanden Borre, J.; Mucher, S. Heathland conservation status mapping through integration of hyperspectral mixture analysis and decision tree classifiers. *Remote Sens. Environ.* **2012**, *126*, 222—231.
11. Kemker, R.; Salvaggio, C.; Kanan, C. Algorithms for semantic segmentation of multispectral remote sensing imagery using deep learning. *ISPRS J. Photogramm. Remote Sens.* **2018**, *145*, 60–77.
12. Pirotti, F.; Sunar, F.; Piragnolo, M. Benchmark of machine learning methods for classification of a sentinel-2 image. In Proceedings of the XXIII ISPRS Congress, Prague, Czech Republic, 12–19 July 2016.
13. Mateo-García, G.; Gómez-Chova, L.; Camps-Valls, G. Convolutional neural networks for multispectral image cloud masking. In Proceedings of the IGARSS, Fort Worth, TX, USA, 23–28 July 2017.
14. Guo, X.; Huang, X.; Zhang, L.; Zhang, L.; Plaza, A.; Benediktsson, J. A. Support Tensor Machines for Classification of Hyperspectral Remote Sensing Imagery. *IEEE Trans. Geosci. Remote Sens.* **2016**, *54*, 3248–3264.
15. Cichocki, A.; Mandic, D.; De Lathauwer, L.; Zhou, G.; Zhao, Q.; Caiafa, C.; Phan, H. Tensor Decompositions for Signal Processing Applications: From two-way to multiway component analysis. *IEEE Signal Process. Mag.* **2015**, *32*, 145–163.
16. Jolliffe, I.T. *Principal Component Analysis*, 2nd ed.; Springer Verlag: New York, NY, USA, 2002.
17. Kolda, T.; Bader, B. Tensor Decompositions and Applications. *SIAM Rev.* **2009**, *51*, 455–500.
18. Lopez, J.; Santos, S.; Torres, D.; Atzberger, C. Convolutional Neural Networks for Semantic Segmentation of Multispectral Remote Sensing Images. In Proceedings of the LATINCOM, Guadalajara, Mexico, 14–16 November 2018.
19. European Space Agency. Available online: https://sentinel.esa.int/web/sentinel/missions/sentinel-2 (accessed on 15 July 2019).
20. Kemker, R.; Kanan, C. Deep Neural Networks for Semantic Segmentation of Multispectral Remote Sensing Imagery. *arXiv* **2017**, arXiv:abs/1703.06452.
21. Hamida, A.; Benoît, A.; Lambert, P.; Klein, L.; Amar, C.; Audebert, N.; Lefèvre, S. Deep learning for semantic segmentation of remote sensing images with rich spectral content. In Proceedings of the IGARSS, Fort Worth, TX, USA, 23–28 July 2017.
22. Wang, Q.; Lin, J.; Yuan, Y. Salient Band Selection for Hyperspectral Image Classification via Manifold Ranking. *IEEE Trans. Neural Netw. Learn. Syst.* **2016**, *27*, 1279–1289.
23. Li, S.; Qiu, J.; Yang, X.; Liu, H.; Wan, D.; Zhu. Y. A novel approach to hyperspectral band selection based on spectral shape similarity analysis and fast branch and bound search. *Eng. Appl. Artif. Intell.* **2014**, *27*, 241–250.

24. Zhang. L.; Zhang, L.; Tao, D.; Huang, X.; Du, B. Compression of hyperspectral remote sensing images by tensor approach. *Neurocomputing* **2015**, *147*, 358–363.
25. Astrid, M.; Lee, Seung-Ik. CP-decomposition with Tensor Power Method for Convolutional Neural Networks compression. In Proceedings of the BigComp, Jeju, Korea, 13–16 February 2017.
26. Chien, J.; Bao, Y. Tensor-factorized neural networks. *IEEE Trans. Neural Networks Learn. Syst.* **2018**, *29*, 1998–2011.
27. An, J.; Lei, J.; Song, Y.; Zhang, X.; Guo J. Tensor Based Multiscale Low Rank Decomposition for Hyperspectral Images Dimensionality Reductio. *Remote Sens.* **2019**, *11*, 1485.
28. Li, J.; Liu, Z. Multispectral Transforms Using Convolution Neural Networks for Remote Sensing Multispectral Image Compression. *Remote Sens.* **2019**, *11*, 759.
29. An, J.; Song, Y.; Guo, Y.; Ma, X.; Zhang, X. Tensor Discriminant Analysis via Compact Feature Representation for Hyperspectral Images Dimensionality Reduction. *Remote Sens.* **2019**, *11*, 1822.
30. Absil, P.-A.; Mahony, R.; Sepulchre, R. *Optimization Algorithms on Matrix Manifolds*, 1st ed.; Princeton University Press: Princeton, NJ, USA, 2007.
31. De Lathauwer, L.; De Moor, B.; Vandewalle, J. On the best rank-1 and rank-(R 1 ,R 2 ,⋯,R N) approximation of higher-order tensors. *SIAM J. Matrix Anal. Appl.* **2000**, *21*, 1324–1342.
32. Goodfellow, I.; Bengio, Y.; Courville, A. *Deep Learning*, 1st ed.; MIT Press, 2016.
33. Sheehan, B. N.; Saad, Y. Higher Order Orthogonal Iteration of Tensors (HOOI) and its Relation to PCA and GLRAM. In Proceedings of the 7th SIAM International Conference on Data Mining, Minneapolis, MN, USA, 26–28 April 2007.
34. Badrinarayanan, V.; Kendall, A.; Cipolla, R. SegNet: A Deep Convolutional Encoder-Decoder Architecture for Image Segmentation. *IEEE Trans. Pattern Anal. Mach. Intell.* **2017**, *39*, 2481–2495.
35. De Lathauwer, L.; De Moor, B.; Vandewalle, J. A Multilinear Singular Value Decomposition. *SIAM J. Matrix Anal. Appl.* **2000**, *21*, 1253–1278.
36. Rodes, I.; Inglada, J.; Hagolle, O.; Dejoux, J.; Dedieu, G. Sampling strategies for unsupervised classification of multitemporal high resolution optical images over very large areas. In Proceedings of the 2012 IEEE International Geoscience and Remote Sensing Symposium, Munich, Germany, 22–27 July 2012.

Sample Availability: Samples of the compounds ..... are available from the authors.